

# Controlling the Mechanism of Nucleation and Growth Enables Synthesis of UiO-66 Metal–Organic Framework with Desired Macroscopic Properties

Mikalai A. Artsiusheuski, Nicola P. M. Casati, Adam H. Clark, Maarten Nachtegaal, René Verel, Jeroen A. van Bokhoven, and Vitaly L. Sushkevich\*

**Abstract:** By combining in situ X-ray diffraction, Zr K-edge X-ray absorption spectroscopy and  $^1\text{H}$  and  $^{13}\text{C}$  nuclear magnetic resonance (NMR) spectroscopy, we show that the properties of the final MOF are influenced by  $\text{H}_2\text{O}$  and  $\text{HCl}$  via affecting the nucleation and crystal growth at the molecular level. The nucleation implies hydrolysis of monomeric zirconium chloride complexes into zirconium-oxo species, and this process is promoted by  $\text{H}_2\text{O}$  and inhibited by  $\text{HCl}$ , allowing to control crystal size by adjusting  $\text{H}_2\text{O}/\text{Zr}$  and  $\text{HCl}/\text{Zr}$  ratios. The rate-determining step of crystal growth is represented by the condensation of monomeric and oligomeric zirconium-oxo species into clusters, or nodes, with the structure identical to that in secondary building units (SBU) of UiO-66 framework. The rapid crystallization in the absence of  $\text{HCl}$  leads to formation of defective secondary building units with missing zirconium atoms, providing a pathway to control the number of defects in UiO-66 crystals. Remarkably, we have shown that assembling of the metal nodes and linkers into the UiO-66 structure is not the rate-limiting step, and the degree of deprotonation of the linker has no direct effect on the crystallization kinetics or crystal size of product.

## Introduction

Metal–organic frameworks (MOFs) are materials composed of metal-containing nodes connected with organic linkers forming microporous or mesoporous crystal structures.<sup>[1–3]</sup> MOFs demonstrate extremely high pore volume and surface area, and the topology and chemical properties of MOFs can be tuned in a wide range by varying structures of linkers or metal-containing nodes.<sup>[4,5]</sup> These unique features justify a great interest to MOFs for potential applications in different areas such as gas storage and separation,<sup>[6–8]</sup> catalysis,<sup>[9]</sup> electrochemistry,<sup>[10]</sup> and biomedicine.<sup>[11]</sup>

Among numerous MOFs, the UiO-66 framework consisting of  $[\text{Zr}_6(\text{OH})_4\text{O}_4]^{12+}$  oxo-clusters as nodes and terephthalate linkers, which are interconnected forming a cubic structure,<sup>[12]</sup> is one of the most widely studied.<sup>[13–15]</sup> A generally used protocol for the synthesis of UiO-66 MOF

implies crystallization from the *N,N*-dimethylformamide (DMF) solution containing zirconium ( $\text{Zr}^{4+}$ ) or zirconyl ( $\text{ZrO}^{2+}$ ) ions and terephthalic acid in the presence of water and/or aqueous hydrochloric acid modulators at elevated temperatures.<sup>[12,16,17]</sup> The composition of the initial synthetic mixture and the synthetic conditions strongly affect the kinetics of crystallization, as well as properties of the final MOF, such as extent of crystallinity, crystal size and shape and the presence of defects. Ragon et al. showed that addition of aqueous hydrochloric acid and water accelerates crystallization and leads to the formation of smaller UiO-66 crystals.<sup>[18]</sup> Similar trends were also reported by Qui et al.<sup>[17]</sup> Chu et al.<sup>[19]</sup> demonstrated that the presence of aqueous hydrochloric acid also leads to a MOF product with a higher number of defects thus affecting the sorption and catalytic performance. However, what is the role  $\text{H}_2\text{O}$  and  $\text{HCl}$  modulators on the nucleation and crystallization mechanism and how this in turn affects the properties of the final product is still unknown.

Determining the role of modulators in the synthesis of UiO-66 (and any other MOF) is challenging. Many compounds, i.e. zirconium-containing precursors, linker, solvent and modulators, participate in the UiO-66 synthesis, and possible reactions between all these components yield a complex and entangled network of chemical transformations.<sup>[15,20]</sup> This in turn results in the under-exploration of establishing MOF crystallization mechanisms. Several research papers have tracked the formation of the crystalline phase, with X-ray diffraction being the primary technique for this purpose.<sup>[18,21,22]</sup> UiO-66 crystal phase formation is commonly described in terms of nucleation and crystal growth,<sup>[15,20,23]</sup> and the kinetics of crystallization is

[\*] M. A. Artsiusheuski

Laboratory for the Science and Applications of Catalysis, College of Chemistry, University of California at Berkeley: 275 Tan Hall, Berkeley, CA, USA, 94720

N. P. M. Casati, A. H. Clark, M. Nachtegaal

Paul Scherrer Institute, Center for Photon Science, 5232 Villigen PSI, Switzerland

M. Nachtegaal, J. A. van Bokhoven, V. L. Sushkevich

Paul Scherrer Institute, Center for Energy and Environmental Sciences, 5232 Villigen PSI, Switzerland

+ 41563103518

E-mail: vitaly.sushkevich@psi.ch

R. Verel, J. A. van Bokhoven

Institute for Chemistry and Bioengineering, ETH Zurich, Vladimir-Prelog-Weg 1, 8093 Zurich, Switzerland

fitted using Avrami-Erofeev,<sup>[24]</sup> Sharp–Hancock<sup>[25]</sup> and Gualtieri<sup>[26]</sup> models. Notably, it has been shown that the kinetics of crystallization can be affected by the addition of modulators.<sup>[18]</sup> Up to date it remains an empiric observation and there is no fundamental understanding of how these modulators affect the synthesis mechanism. One of the reasons for that is the lack of understanding of chemical transformations taking place in solution, i.e. the non-crystalline transformations, specifically during the induction period. Due to the absence of any crystalline or amorphous solid phase, these parts of synthesis cannot be investigated by X-ray diffraction techniques alone. Hu et al. applied in situ pair distribution function analysis of X-ray scattering data and showed that zirconium nodes are formed and present in the synthetic solution during UiO-66 synthesis.<sup>[27]</sup> However, it is currently unknown how the preformed building units from the mother liquid contribute to either nucleation or crystal growth stages of crystallization. To comprehensively describe the mechanism of UiO-66 (and any other solid) synthesis, a combination of methods that allow to monitor the dynamics of species in solution as well as tracking amorphous and crystalline solid formation is required.<sup>[23]</sup>

We have previously applied a combination of in situ electrospray ionization coupled with high-resolution mass spectrometry (ESI-HRMS), magic angle spinning NMR (MAS NMR) and X-ray diffraction (XRD) to study the synthesis mechanism of MOFs<sup>[28]</sup> and have recently applied it to UiO-66 crystallization.<sup>[29]</sup> Briefly, we revealed that the UiO-66 synthesis involves depolymerization of zirconium tetrachloride leading to zirconium chloroterephthalates and the formation of zirconium-oxo nodes coordinated by terephthalate linkers followed by assembling of nodes and linkers into a three-dimensional structure. It is important to develop methods to control the relative rates of these reactions to, in turn, regulate crystallization kinetics and macroscopic properties of the final product, such as crystal size and the presence of defects. As discussed above, the addition of modulators, i.e. water and hydrochloric acid, can be applied for this purpose. However, the effect of modulators is still a subject of significant debate: while in some reports the acceleration of crystallization is attributed to H<sub>2</sub>O,<sup>[30]</sup> other studies suggest that this is due to HCl.<sup>[18]</sup> Therefore, determining the effect of each modulator and establishing the mechanism of their acting require a comprehensive study.<sup>[20,31]</sup> Moreover, several key aspects of UiO-66 synthesis remain unclear, also in our previous study. The formation of the secondary building units (i.e., zirconium-oxo nodes) from zirconium chloride precursor stoichiometrically requires an oxygen source, hence implying hydrolysis reaction. The hydrolysis process is generally induced by water and can be affected by the presence of acid. Determining the role of water is of utmost importance given the emergence of water as the primary solvent in large scale UiO-66 synthesis.<sup>[15]</sup> It is worth noting that the effect of H<sub>2</sub>O and HCl modulators on the presence of defects in UiO-66 structure is understudied,<sup>[31]</sup> yet this aspect is critical for application of these materials.<sup>[32,33]</sup>

In this contribution, we investigated UiO-66 crystallization from various initial synthetic mixtures containing zirconium tetrachloride and terephthalic acid dissolved in dimethylformamide with the addition of water and/or hydrochloric acid modulators, where the HCl/Zr ratio ranges between 0 and 11 and the H<sub>2</sub>O/Zr ratio between 11 and 40. We applied a combination of in situ X-ray diffraction (XRD), Zr K-edge X-ray absorption spectroscopy (XAS), and <sup>1</sup>H and <sup>13</sup>C NMR spectroscopy to comprehensively study the kinetics of crystallization and track chemical transformations on molecular level, and correlated these results with macroscopic properties of UiO-66 MOF products, such as crystal size and porous properties. This approach allowed us to reveal the mechanism of action of acidic modulator and water. We show that the addition of modulators allows for controlling the crystal size of the final products in a range of 35 nm to 130 nm. The dissolution of zirconium tetrachloride in the linker-containing DMF initially yields monomeric zirconium chloroterephthalate octahedral complexes. These complexes are hydrolyzed to monomeric and oligomeric zirconium-oxo octahedral species, where further condensation leads to the formation of [Zr<sub>6</sub>(OH)<sub>4</sub>O<sub>4</sub>] nodes. Notably, at low HCl/Zr ratio these nodes are formed with defects represented by missing zirconium atoms in the structure. However, these defect nodes also crystallize to the UiO-66 structure. The comparison of kinetic data from XAS and XRD suggests that the hydrolysis of zirconium chloride monomers corresponds to the nucleation stage, while the condensation of monomeric and oligomeric zirconium-containing species into zirconium nodes is the rate-limiting step of crystal growth. Interestingly, we show that crystal growth is not limited by the reaction of linkers with nodes, therefore the degree of (de)protonation of terephthalic acid has no pronounced effect on the synthesis kinetics. The here revealed details of the UiO-66 crystallization mechanism are essential for the development of efficient protocols to synthesize MOFs with the desired crystal size and amounts of defects. The proposed methodology has a potential to be extended on synthesis of other MOFs and beyond.

## Results and Discussion

Synthesis of UiO-66 was investigated using initial synthetic mixtures containing fixed amounts of zirconium tetrachloride (ZrCl<sub>4</sub>) and terephthalic acid dissolved in N,N-dimethylformamide with specific amounts of hydrochloric acid and water added. Two different series of synthetic mixtures were studied: Series 1 with different amounts of 37 wt% aqueous hydrochloric acid added and Series 2 with fixed amounts of hydrochloric acid with different HCl concentrations, prepared by diluting the 37 wt% aqueous hydrochloric with water (described in detail in Table S1). This allowed for an independent systematic variation of H<sub>2</sub>O/Zr and HCl/Zr ratios to disentangle the effects of H<sub>2</sub>O and HCl on the mechanism and kinetics of UiO-66 crystallization. Synthetic solutions and corresponding resulting MOFs are denoted as UiO-66(X,Y) where X and Y are the initial H<sub>2</sub>O/Zr and

HCl/Zr ratios in the synthetic mixture, respectively. Zr/H<sub>2</sub>O and Zr/HCl ratios in the initial synthetic mixtures used for synthesis of UiO-66 materials, and crystal size and micro-pore volumes of UiO-66 products are summarized in Table 1.

According to results of nitrogen physisorption (Table 1, Figure S1), samples corresponding to Series 1 (UiO-66 (11, 3.0); UiO-66 (20, 5.5); UiO-66 (30, 8.3) and UiO-66 (40,11.0)) have similar total pore volumes of between 0.5 and 0.6 cm<sup>3</sup>·g<sup>-1</sup>, which is characteristic of UiO-66 material. Notably, decrease in HCl/Zr ratio below 5.5 at constant H<sub>2</sub>O/Zr=40 ratio (Series 2) leads to product with lower pore volume. We suggest that this is an effect of the formation of UiO-66 material with smaller crystal size and, possibly, lower extent of crystallinity (*vide infra*).

Figure 1 shows SEM images of UiO-66 products obtained after solvothermal crystallization at 343 K using initial synthetic solutions with different composition. All UiO-66 products consist of aggregated nanocrystals, typical of UiO-66 synthesis under those conditions.<sup>[17,19,34]</sup> However, initial synthetic composition affects the sizes of the product, as summarized in Table 1, Figures 1, S2 and S3. The simultaneous increase of HCl/Zr and H<sub>2</sub>O/Zr ratios at fixed HCl/H<sub>2</sub>O, Series 1 (Table 1, Figure 1, upper part) leads to a slight decrease in crystallite average size. In contrast, the decrease in HCl/Zr ratio at constant H<sub>2</sub>O/Zr ratio, Series 2 (Table 1, Figure 1, lower part), gradually leads to smaller crystals: from 110 nm for UiO-66 (40, 11.0) to 35 nm for UiO-66 (40, 0).

According to the crystal growth theory, which is generally applied to MOFs crystallization,<sup>[20,23]</sup> the crystal size is determined by the ratio between the rates of nucleation and crystal growth. The variation of the crystal size for different synthetic mixtures points to an effect of HCl/Zr and H<sub>2</sub>O/Zr ratios on the nucleation and crystal growth processes, further investigated by means of time-resolved in situ X-ray diffraction. Figure 2A shows exemplary time evolution profiles of X-ray diffractograms during UiO-66 crystallization. Upon reaction, patterns characteristic of UiO-66 with most intense Bragg (111) and (002) reflections located at 2 $\theta$  of 2.35 ° and 2.71 °, respectively, appear. Notably, the background shape and intensity remain constant during the synthesis, indicating that the formation of any substantial quantities of amorphous solid phases is highly unlikely. Figures 2 B and C show the extent of crystallinity versus crystallization time for Series 1 and 2, respectively. The kinetic curves exhibit a typical S-shape as reported for MOF crystallization, with an initial induction period followed by a progressive evolution leading to the crystalline phase.<sup>[20,23]</sup> The Gualtieri<sup>[26]</sup> model was used to model the UiO-66 crystallization kinetics enabling a quantitative estimation of kinetic constants corresponding to nucleation and growth processes. According to the model, the temporal evolution of crystalline UiO-66 is described as follows:

$$\alpha = \frac{1}{1 + e^{-\frac{t-a}{b}}} \left( 1 - e^{-(k_{\text{growth}} \cdot t)^n} \right)$$

**Table 1:** Zr/H<sub>2</sub>O and Zr/HCl ratios in the initial synthetic mixtures and crystal size and total pore volumes of UiO-66 products.

Sample Parameter	Series 1				Series 2				
	UiO-66 (11, 3.0)	UiO-66 (20, 5.5)	UiO-66 (30, 8.3)	UiO-66 (40,11.0)	UiO-66 (40, 8.3)	UiO-66 (40, 5.5)	UiO-66 (40, 2.7)	UiO-66 (40, 1.4)	UiO-66 (40, 0.0)
H <sub>2</sub> O/Zr in initial synthetic mixture	11	20	30	40	1.3(3)	1.6(3)	1.3(3)	40	40
HCl/Zr in initial synthetic mixture	3.0	5.5	8.3	11.0	8.3	5.5	2.7	1.4	0
Mean crystal size from SEM, nm	128	127	122	110	97	78	74	51	35
Total pore volume, cm <sup>3</sup> ·g <sup>-1</sup>	–	0.57	0.51	0.61	0.58	0.51	0.37	0.27	0.22

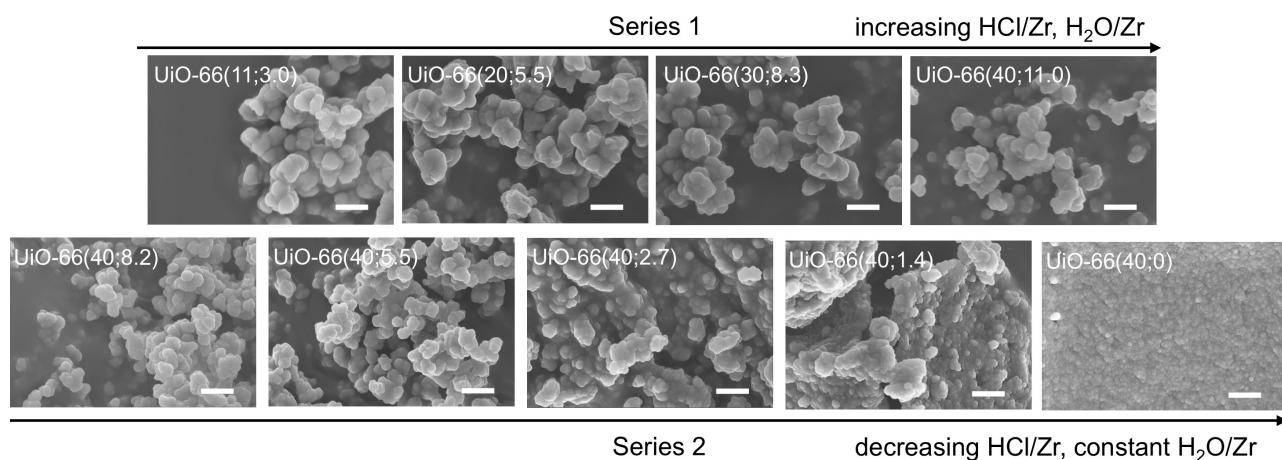


**Figure 1.** SEM images of UiO-66 obtained by solvothermal crystallization using different initial synthetic mixtures. The scale bar corresponds to 300 nm.

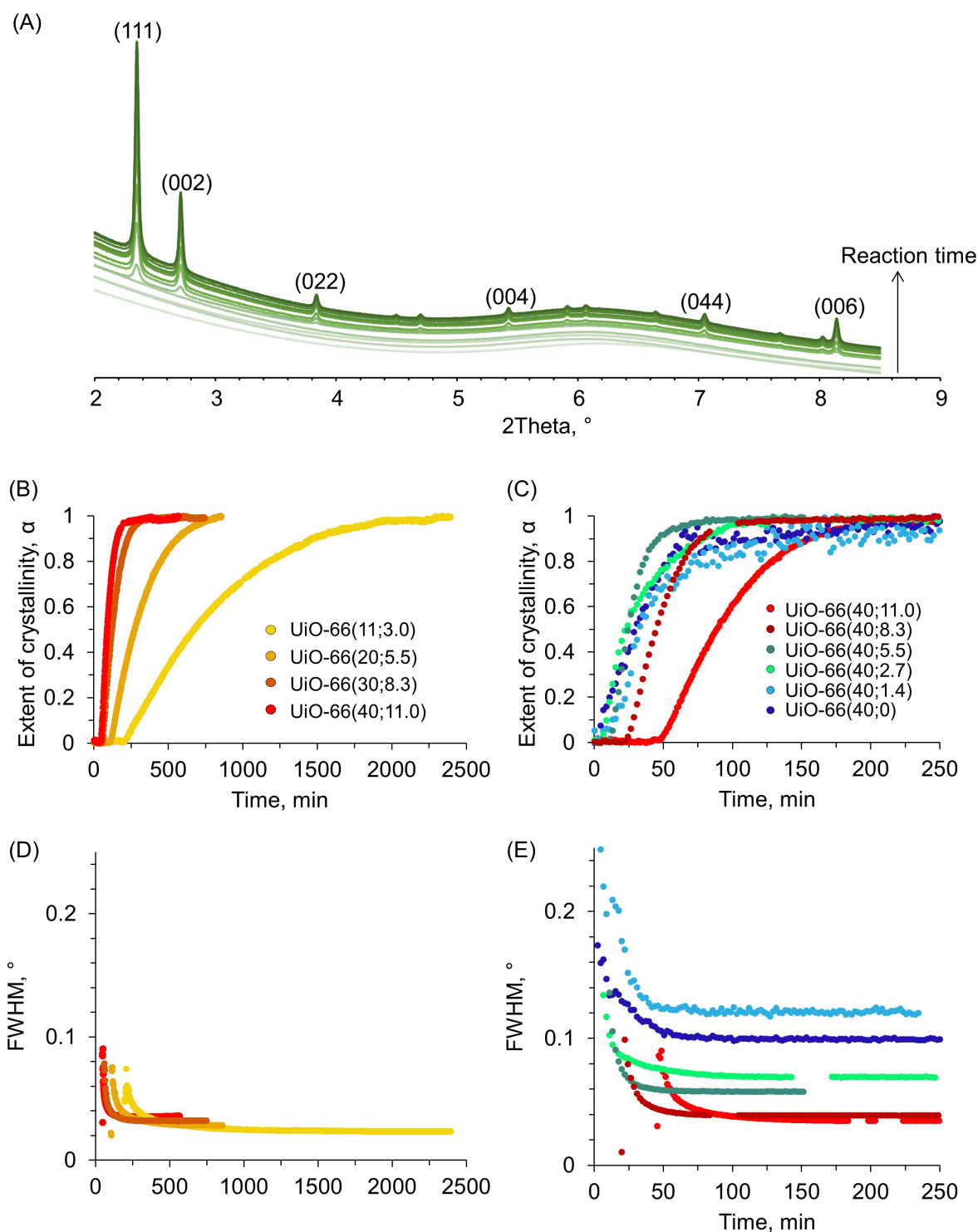


**Figure 2.** Time-resolved XRD data acquired during the synthesis of UiO-66 (40, 11.0) (A), temporal evolution of the extent of UiO-66 crystallinity obtained from XRD data for UiO-66 synthesis from different initial synthetic mixtures corresponding to Series 1 (B) and Series 2 (C); temporal evolution of the full width at half maximum (FWHM) for the (111) Bragg peak during synthesis of UiO-66 from initial synthetic mixtures corresponding to Series 1 (D) and Series 2 (E).

where  $\alpha$  is the extent of crystallinity,  $t$  corresponds to the reaction time,  $k_{growth}$  is the rate constant for growth,  $a$  is the reciprocal rate constant for nucleation,  $k_{nucleation} = \frac{1}{a}$ ,  $b$  is the variance of the nucleation probability distribution and  $n$

represent the dimensionality of crystal growth. Fitted curves are presented in Figure S4, and best-fit parameters are summarized in Table S2.

Time-resolved XRD data corresponding to Series 1 (Figure 2 B) demonstrates that an increase in the amount of added aqueous hydrochloric acid significantly accelerates the crystallization process. The duration of the induction period decreases from 200 min for UiO-66(11, 3.0) to less than 50 minutes for UiO-66(40, 11.0). Similarly, for UiO-66(11, 3.0) more than 2000 minutes were required to reach 90% crystallinity, while for UiO-66(40, 11.0) the same extent of crystallinity is obtained already after 150 minutes. Analysis using the Gualtieri model shows a gradual simultaneous increase in growth constant  $k_{\text{growth}}$  from  $1.2 \cdot 10^{-3}$  to  $1.1 \cdot 10^{-2} \text{ min}^{-1}$  and nucleation constant from  $3.7 \cdot 10^{-3}$  to  $1.4 \cdot 10^{-2} \text{ min}^{-1}$  when increasing the HCl/Zr and H<sub>2</sub>O/Zr ratios from UiO-66(11, 3.0) to UiO-66(40, 11.0) (Table S2). For Series 2, the XRD crystallization kinetic data points to even faster UiO-66 crystallization upon decrease in HCl/Zr ratio at constant H<sub>2</sub>O/Zr ratio of 40 (Figure 2 C). Thus, the induction period and time required to reach 90% crystallinity decreases from 50 min and 150 min, respectively, for UiO-66(40, 11.0) to less than 5 min and 50 min for UiO-66(40, 0.0). Equally, the calculated values of  $k_{\text{growth}}$  and  $k_{\text{nucleation}}$  increase from  $1.1 \cdot 10^{-2}$  and  $1.4 \cdot 10^{-2} \text{ min}^{-1}$  for UiO-66(40, 11.0) to  $4.5 \cdot 10^{-2}$  and  $1.4 \cdot 10^{-1} \text{ min}^{-1}$  for UiO-66(40, 0.0). This points to a promoting effect of H<sub>2</sub>O and an inhibiting effect of HCl on both the nucleation and crystal growth processes.

The evolution of the full width at half maximum (FWHM) parameter for the most intense (111) Bragg reflection was monitored during the crystallization process (Figures 2 D and E for Series 1 and 2, respectively). Shortly after the end of the induction period and the start of the formation of the crystal phase, the FWHM continuously decreases with increasing reaction time and stabilizes at a values between 0.02 and 0.13°. The FWHM reaches stable values coinciding with the reaction time required to reach unity crystallinity. Interestingly, the FWHM final values are very different for the two studied series. For Series 1, all FWHM values are relatively close, with a slight gradual increase from 0.024° for UiO-66(11, 3.0) to 0.035° for UiO-66(40, 11.0), presumably pointing to the smaller average size of the crystals in the latter sample (Figures 1, S2 and S3). In contrast, in the case of Series 2, the FWHM values after complete crystallization significantly increases with a decreasing HCl/Zr ratio: from 0.035° for UiO-66(40, 11.0) to 0.10° for UiO-66(40, 0.0). The higher values of the FWHM originate from smaller crystal size, in line with the results of SEM (Figure 1, S2 and S3). Possibly, the FWHM of the materials corresponding to Series 2 is larger due to the lower extent of crystallinity. While the FWHM parameter is frequently utilized to determine crystallite size, in the simplest way using Sherrer equation, such an analysis requires excluding other factors of peak broadening, such as instrumental broadening, inhomogeneous strain, crystal lattice imperfections, different degree of crystallinity etc.<sup>[35]</sup> Notably, the results of SEM analysis show same trend of decrease of particle size with decreasing HCl/Zr ratio in Series 2 (Figures 1, S2 and S3, Table 1).

The structural evolution of zirconium-containing species during UiO-66 synthesis was studied by means of Zr K-edge

X-ray absorption spectroscopy. Figure S5 shows an exemplary time-resolved Zr K-edge X-ray absorption near edge structure (XANES) and extended X-ray absorption fine structure (EXAFS) spectra series acquired during UiO-66 crystallization. The spectra change significantly during the reaction, indicating changes of the zirconium-containing species. The time-resolved datasets were deconvoluted into spectral domains using principal component analysis (PCA).<sup>[36,37]</sup> For the Series 1, three linearly independent components are required to describe the evolution of the XAS spectra during crystallization (Figure S6), named Principal Components 1, 2 and 3 (designated as PC1, PC2 and PC3, respectively), in line with previous report.<sup>[29]</sup> Figure 3 summarizes the results of the PCA of the spectra acquired for Series 1: subfigures A), D) and G) depict XANES spectra corresponding to PC1, PC2 and PC3, respectively, subfigures B), E) and H) present the corresponding non-phase corrected  $k^3$ -weighted Fourier transformed EXAFS (FT EXAFS) spectra, and subfigures C), F) and I) demonstrate the temporal evolution of the different components during crystallization.

Both Zr K-edge XANES and FT EXAFS spectra of every principal component determined from each initial synthetic mixture in the Series 1 are statistically identical. A significant difference in their temporal evolution was observed. XANES spectra corresponding to PC1 possess three resolved peaks at 18015, 18023, and 18032 eV and resemble that of bulk zirconium (IV) chloride (Figure S8). The Zr K-edge FT EXAFS spectra of PC1 contain one single peak located at about 2 Å radial distance (not phase corrected). The absence of other signals at higher radial distances suggests that zirconium-containing species corresponding to PC1 possess monomeric nature. In our previous work we have shown that zirconium chloroterephthalates are formed at the initial stages of the synthesis.<sup>[29]</sup> Therefore, a model comprising the presence of oxygen and chloride scatterers in the first coordination sphere was utilized to quantitatively fit the data. The analysis reveals the presence of  $1.5 \pm 0.4$  oxygen and  $4.7 \pm 0.5$  chloride scatterers located at a distances of  $2.18 \pm 0.02$  Å and  $2.46 \pm 0.01$  Å, respectively (Table S3, Figure S9). The total coordination number is close to 6, which is typical for Zr<sup>4+</sup> octahedral complexes in organic solutions.<sup>[28]</sup>

Zr K-edge XANES spectra corresponding to PC2 differ from the spectra of any of the standard compounds (such as ZrO<sub>2</sub>, ZrCl<sub>4</sub>, UiO-66), indicating a unique environment of the zirconium atoms (Figure S8). The intensity of the peak in the first coordination sphere in the Zr K-edge FT EXAFS spectra of PC2 is slightly lower than that in the spectra of PC1. At the same time, a weak signal in the second coordination sphere located at 3.1 Å is visible. The decrease of the intensity of the signal in the first coordination sphere can be associated with either a decrease in the coordination number, formation of a more disordered structures around Zr atoms or change of scatterer type to an element with a lower Z number. The first two reasons are unlikely: i) compounds containing zirconium atoms with a coordination number below six are extremely rare and one cannot expect their formation under the conditions used in the present

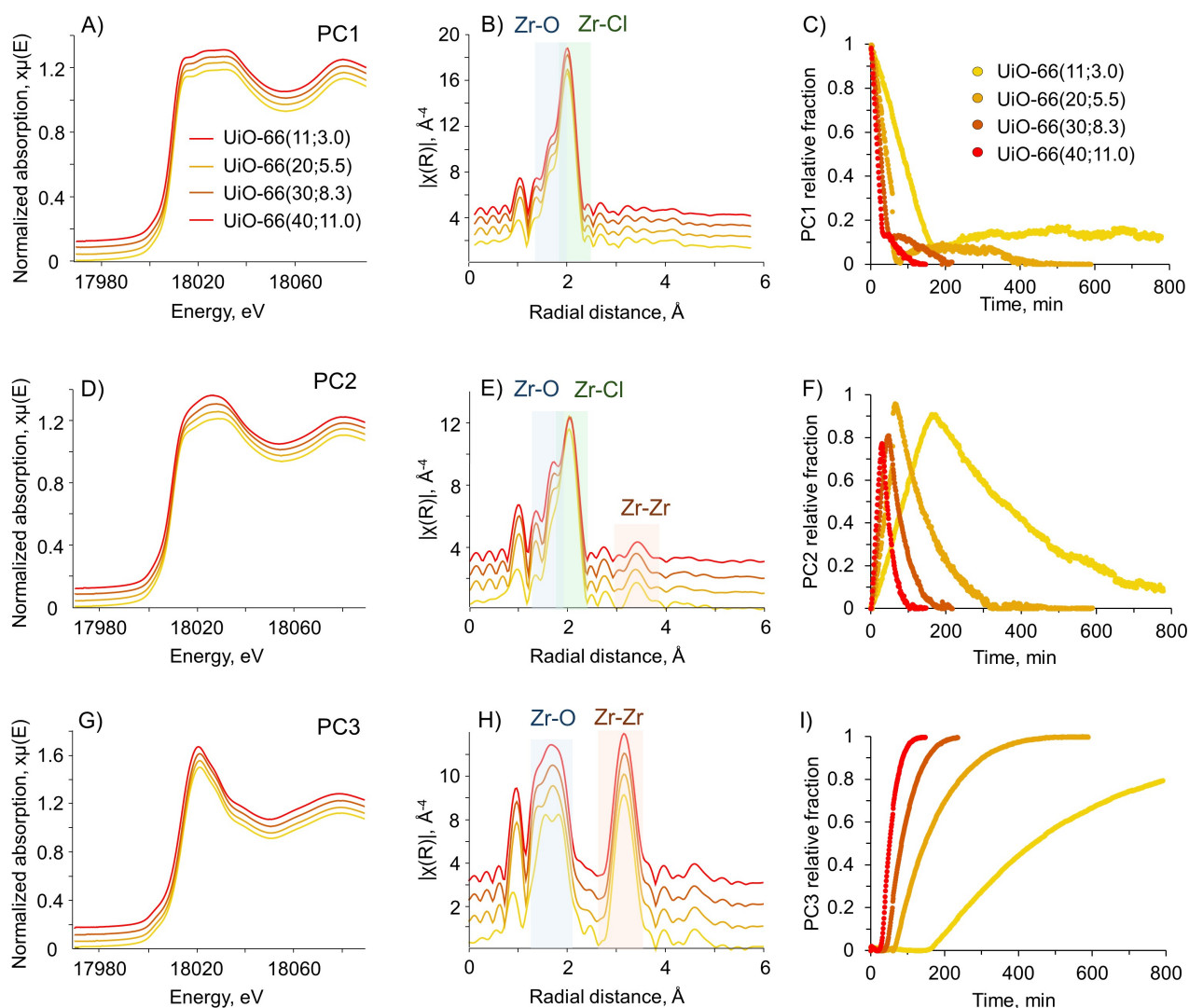


**Figure 3.** The results of the PCA of the Zr K-edge time-resolved datasets of UiO-66 synthesis from different initial synthetic solutions corresponding to Series 1: A), D) and G) depict XANES spectra corresponding to PC1, PC2 and PC3, respectively, B), E) and H) the non-phase corrected  $k^2$ -weighted Fourier transformed EXAFS spectra, and C), F) and I) the temporal evolution of the different components during the crystallization.

study and ii) no formation of a solid phase has been detected at reaction times where PC1→PC2 transformation takes place, therefore Zr-containing species are expected to be monomeric or oligomeric complexes in solution. In contrast, the substitution of chloride atoms with oxygen ones can be anticipated, given the general tendency of zirconium to form Zr–O bonds. To fit the EXAFS data corresponding to PC2, a model comprising a superposition of oxygen and chlorine scatterers in the first coordination sphere and zirconium scatterer in the second coordination sphere was utilized. The results of fitting show the coordination numbers of  $5.1 \pm 0.5$ ,  $1.3 \pm 0.5$  and  $0.6 \pm 0.2$  and distances to the scatterers of  $2.33 \pm 0.01$  Å,  $2.54 \pm 0.01$  Å,  $3.72 \pm 0.01$  Å for Zr–O, Zr–Cl and Zr–Zr scattering paths, respectively (Table S3, Figure S10). The decrease in the coordination number corresponding to chlorine and simultaneous increase in the coordination number due to oxygen indicates the ligand substitution from chloride to oxygen-containing ligands

(terephthalate, H<sub>2</sub>O or OH), while the appearance of the Zr–Zr scattering signal in the second coordination sphere points to the formation of dimeric and/or oligomeric species.

Zr K-edge XANES spectra of PC3 are similar to the one of bulk UiO-66 structure (Figure S8). The FT EXAFS spectra of PC2 and PC3 showed significant differences: the intensity of the signal in the first coordination sphere in the spectrum of PC3 was lower and the maximum was shifted by  $\sim 0.2$  Å to lower radial distances, while the intensity of the signal in the second sphere increased significantly. A crystal structure of UiO-66<sup>[12,38,39]</sup> was used as a model for fitting of the PC3 FT EXAFS spectrum (Table S4 and Figure S11). Two distinct Zr–O scattering paths in the first sphere with coordination numbers for oxygen scatterers close to 4 and 6, respectively, and Zr–O distances of  $2.12 \pm 0.02$  Å and  $2.26 \pm 0.01$  Å, respectively, were detected. The values are in a good agreement with literature data of hydroxylated UiO-66 MOF.<sup>[12]</sup> The second coordination sphere consists of Zr

scatterers with the coordination number  $4.7 \pm 1.1$  located  $3.53 \pm 0.01$  Å. These data confirm the presence of  $[\text{Zr}_6\text{O}_4(\text{OH})_4]$  clusters in the UiO-66 structure.<sup>[12]</sup>

The dataset corresponding to Series 2 (Figure 4) significantly differs from that of Series 1. While for the initial synthetic mixtures UiO-66 (40, 11.0), UiO-66 (40, 8.3) and UiO-66 (40, 5.5) the principal component analysis shows the presence of three independent components, for other samples with HCl/Zr ratios below 5.5 only two statistically different principal components were extracted (Figure S7). Moreover, both XANES and EXAFS spectra corresponding to PC1 were very different for the samples in Series 2 (Figures 4 A and B). The ones corresponding to UiO-66 (40, 11.0) and UiO-66 (40, 8.3) resemble those of PC1 in Series 1: there are features at 18015, 18023, and 18032 eV in the XANES spectra and intense signal with maximum at 2.0 Å in the FT EXAFS spectra. A decrease in HCl/Zr ratio below

8.3 leads to significant changes in the spectral shape of PC1: in the XANES spectra, the three aforementioned features merge into a single feature at 18020 eV, while in the FT EXAFS spectra the peak located at ca 2.0 Å has lower intensity and has shifted to 1.8 Å with a simultaneous development of a signal at 3.1 Å. These features are characteristic for  $[\text{Zr}_6\text{O}_4(\text{OH})_4]$  clusters.<sup>[12,39]</sup> Linear combination fitting (LCF) shows that spectra of PC1 corresponding to the initial synthetic mixtures in Series 2 with HCl/Zr ratios below 8.3 can be represented as a superposition of PC1 and PC3 spectra determined from UiO-66 (40, 11) sample or from any other sample from Series 1 (Figure S12, Table S5). This indicates that for the samples with low HCl/Zr ratios, the formation of the secondary building units (SBU) of UiO-66 occurs very rapidly. Therefore, the synthetic mixtures with high water content and HCl/Zr ratios below 8.3 contain a substantial fraction of  $[\text{Zr}_6\text{O}_4-$

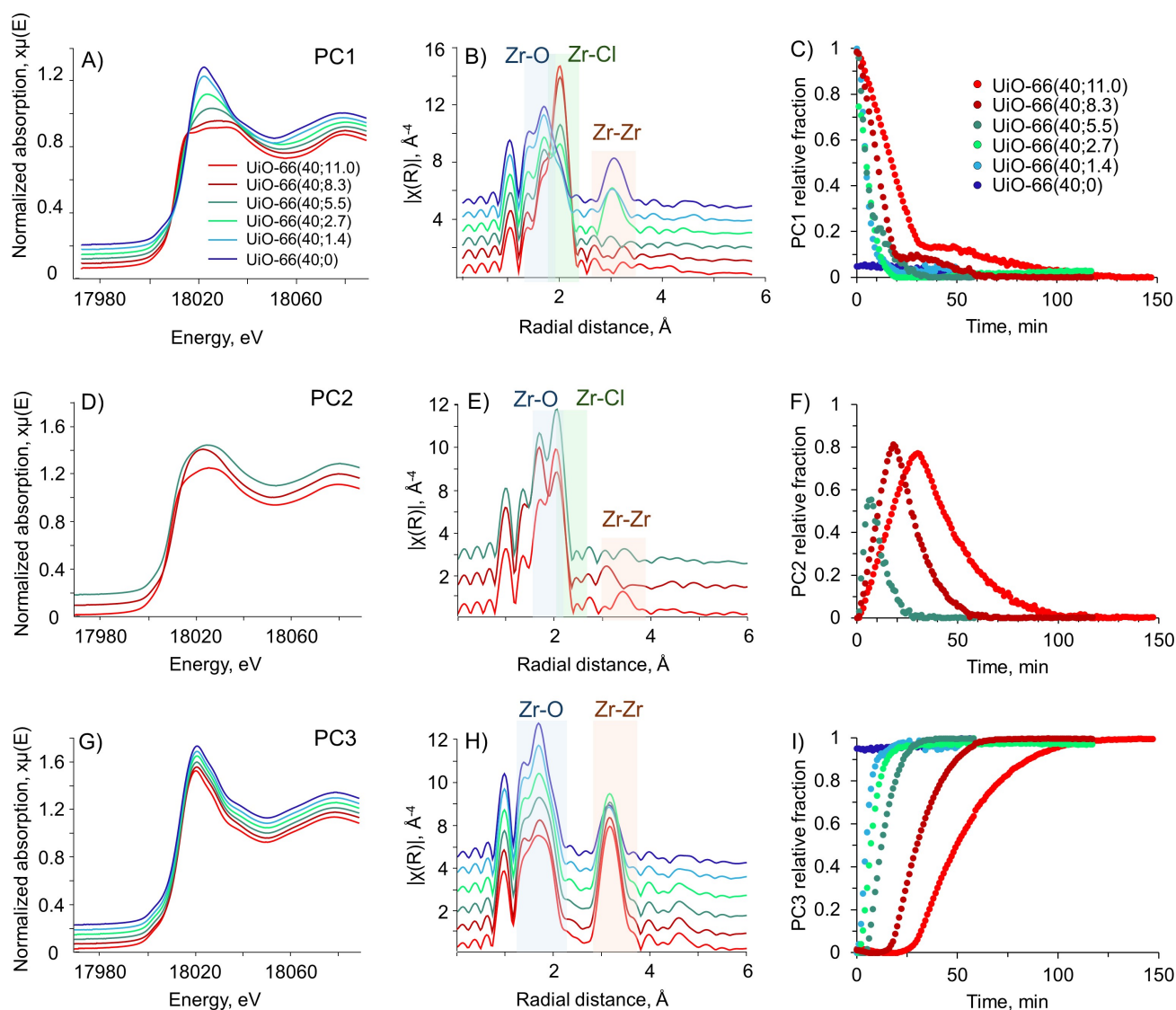


**Figure 4.** The results of the PCA of the Zr K-edge time-resolved datasets of UiO-66 synthesis from different initial synthetic solutions corresponding to Series 2: A), D) and G) depict XANES spectra corresponding to PC1, PC2 and PC3, respectively, B), E) and H) the non-phase corrected  $k^2$ -weighted Fourier transformed EXAFS spectra, and C), F) and I) the temporal evolution of the different components during the crystallization.

(OH)<sub>4</sub>] clusters already at the start of the reaction. The overly fast reaction makes the analysis of XAS spectra corresponding to the initial stages of crystallization ambiguous, and therefore the fitting of PC1 and PC2 FT EXAFS spectra corresponding to Series 2 was omitted. For the same reasons, the analysis of the kinetics of transformation between principal components has been limited to UiO-66 (40, 11), UiO-66 (40, 8.3) and UiO-66 (40, 5.5) samples from Series 2. However, the analysis of XAS spectra of PC3 is still useful to determine the effect of the starting composition on the structure of the final product. The FT EXAFS spectra of PC3 (Figure 4H) possess identical signals at 1.8 Å in the first coordination sphere, that at 3.1 Å is being different: its intensity progressively decreases with a decrease in HCl/Zr ratio. Fitting of the spectra corresponding to PC3 in Series 2 is presented in Table S4 and Figures S13–S17 and shows that no measurable changes occur in the first coordination sphere, yet the coordination number of Zr scatterers in the second sphere decreases from  $4.7 \pm 1.1$  for UiO-66 (40, 11.0) to  $2.3 \pm 1.5$  for UiO-66 (40, 0). This points to the formation of UiO-66 with a high number of defects represented by missing zirconium atoms in the nodes. Notably, the Zr–Zr coordination number in PC3 does not change with the crystallization time, indicating that the formation of nodes is an irreversible process, and the defects of the missing zirconium atoms in the nodes cannot be healed with prolonging the crystallization time. Interestingly, the Zr–Zr distance remains at  $3.53 \pm 0.01$  Å for all samples, indicating that the presence of defects has no measurable effect on interatomic Zr–Zr distances in the nodes. Formation of crystal structure with defects for UiO-66 (40, 2.7), UiO-66 (40, 1.4) and UiO-66 (40, 0) samples was also confirmed by means of FTIR spectroscopy (Figure S19).

Apart from the structural information determined from the analysis of XANES and EXAFS spectra, XAS provides additional mechanistic details of UiO-66 crystallization from the time series of the concentration profiles of the principal components (Table S6). The rates of PC1 transformation into PC2 in both Series 1 and 2 do not change with crystallization time for all samples, indicating that the reaction is zero-order (Figures 3 C and 4 C). In some cases, the rate even increases, which could point to the autocatalytic nature of this reaction step.<sup>[29]</sup> The absolute rate values significantly depend on the starting synthetic mixture composition: in Series 1 the rate increases when both H<sub>2</sub>O/Zr and HCl/Zr ratios increase, and in Series 2 it increases with a decrease in HCl/Zr ratio. From this observation one can conclude that the chemical transformations corresponding to the conversion of PC1 into PC2 are promoted by water and inhibited by HCl. A different picture has been observed for the transformation of PC2 to PC3: this process slows down with crystallization time, indicating a reaction order  $>0$  with respect to zirconium containing species comprising PC2. Remarkably, the initial rate of PC2→PC3 transformation is affected by the synthetic composition in a similar way as the rate of PC1→PC2 transformation: it is accelerated by H<sub>2</sub>O and inhibited by HCl.

The rates of nucleation and crystal growth extracted from XRD linearly increase with an increase in H<sub>2</sub>O/Zr

ratio, while HCl inhibits both these processes, as both nucleation and growth rate constants decrease with increase in HCl/Zr ratio (Figures 5 A and B). A similar behavior is observed for the evolution of principal components in the XAS spectra: rates of both PC1→PC2 and PC2→PC3 conversion are accelerated by H<sub>2</sub>O and inhibited by HCl (Figures 5 C and D). Importantly, an acceleration by water has a stronger effect, and therefore the simple addition of aqueous hydrochloric acid containing 63 wt% of water leads to an apparent increase of hydrolysis rate, which, in turn, promotes crystallization kinetics in general. This may lead to an incorrect conclusion of a promoting effect of HCl molecules on the crystallization, as suggested earlier.<sup>[18]</sup> The experiments where the synthesis has been performed starting from mixtures with fixed H<sub>2</sub>O/Zr ratio and varied HCl/Zr ratio (Series 2) clearly show that HCl has an inhibiting effect, and not a promoting. This is in line with studies of ZrCl<sub>4</sub> hydrolysis and polymerization in water-organic solvents<sup>[40]</sup> and aqueous HClO<sub>4</sub> solutions,<sup>[41,42]</sup> showing similar promoting effects of water and inhibiting effects of the strong mineral acid. Importantly, the effect of HCl on nucleation and growth is different at low HCl/Zr ratios: the nucleation rates are linearly inhibited in the studied range of HCl/Zr ratios, while growth rates are affected insignificantly at HCl/Zr ratios below 5 (Figure 5 B). Thus, at HCl/Zr ratio lower than 5,  $k_{\text{growth}}$  remains unchanged while  $k_{\text{nucleation}}$  increases dramatically, resulting in the UiO-66 with smaller crystal size, evidenced by SEM (Figures 1, S1 and S2) and showing higher FWHM value in XRD (Figures 2 E and 5 F). The discovery of a parameter to control the relative rates of nucleation and growth and, consequently, the crystal size of UiO-66 product, becomes even more substantial considering the identical activation energies for nucleation and crystal growth,<sup>[29]</sup> making variation of synthesis temperature an ineffective tool for this purpose.

Another striking phenomenon observed is the excellent correlations between i) the rates of nucleation extracted from XRD and those of PC1→PC2 conversion (Figure S18A), and ii) between the rates of crystal growth and those of PC2→PC3 conversion (Figure S18B). Given that fact and our recent findings,<sup>[29]</sup> the chemical state described by PC1 corresponds to zirconium chloride and individual chloroterephthalate complexes, PC2 represents a mixture of zirconium-oxo monomeric species with contribution of dimeric and oligomeric species and PC3 is attributed to zirconium-oxo clusters with a structure identical to that of metal-oxo nodes in UiO-66. The nucleation process is mostly a hydrolysis reaction, implying the substitution of chloride ligands with oxygen-containing ones in the first zirconium coordination sphere. Even monomeric zirconium-oxo species can serve as nuclei for crystallization. This is in line with the reports by Taddei et al., showing that aging of the synthetic solution in the presence of water leads to the formation of individual zirconium monomeric species having hydroxyls, DMF molecules and chloride anions as ligands.<sup>[40,41]</sup> These monomeric species can act as efficient nuclei for UiO-66 crystallization.<sup>[43,44]</sup> The monomeric nature of nuclei in UiO-66 synthesis differs from the case of ZIF-67, where formation of oligomeric species is required for

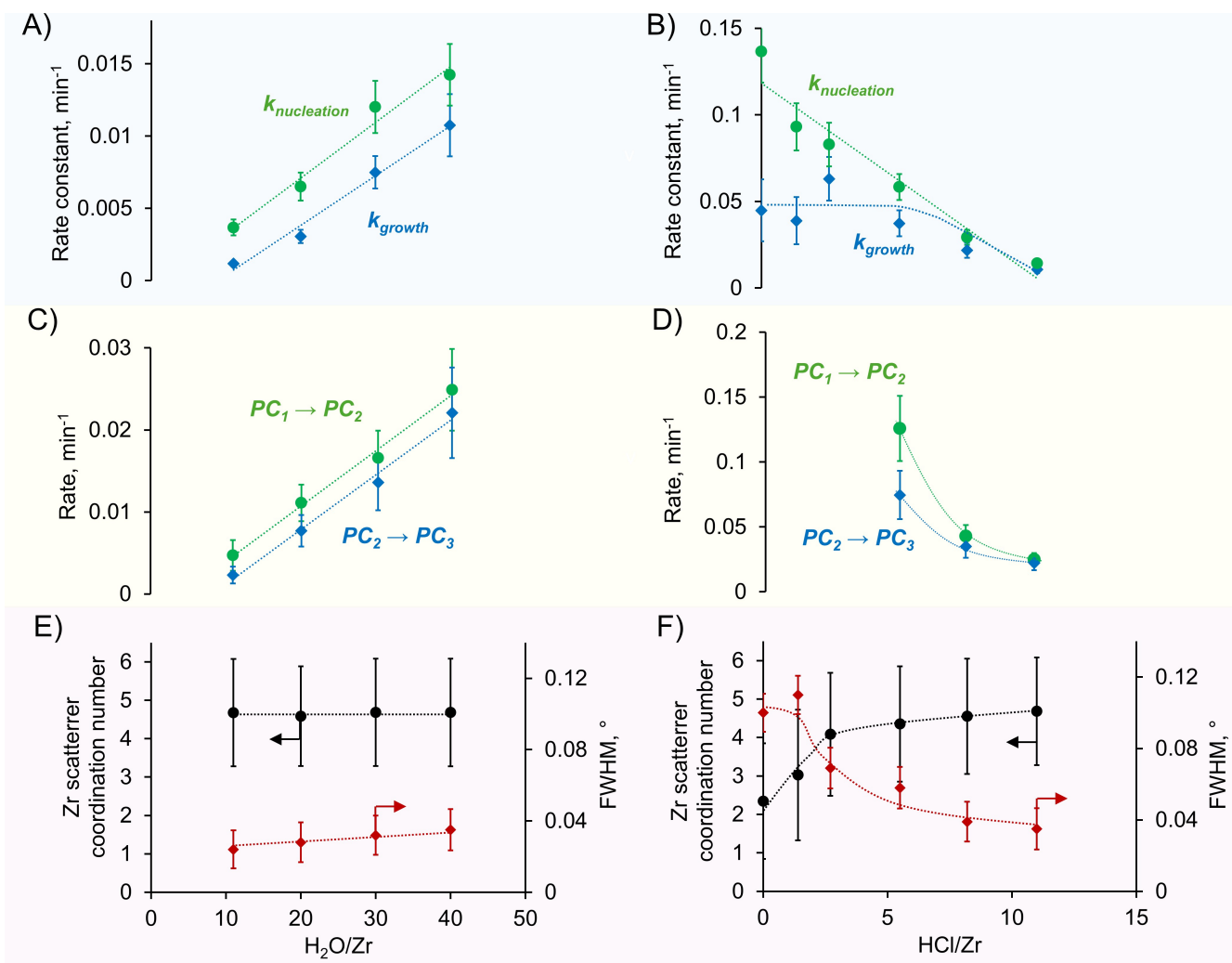


**Figure 5.** The rate constants of nucleation and crystal growth obtained by fitting of in situ XRD data for Series 1 (A) and Series 2 (B), rates of PC1  $\rightarrow$  PC2 and initial rates of PC2  $\rightarrow$  PC3 conversion from in situ XAS data for Series 1 (C) and Series 2 (D); coordination number of Zr scatterer from EXAFS fitting of PC3 component and final full width on half maximum (FWHM) for (111) Bragg peak in XRD for Series 1 (E) and Series 2 (F). Dotted lines are intended to guide the eye, error bars represent 95% confidence interval determined from standard error.

nucleation,<sup>[45]</sup> proving that crystallization of each material should be studied separately and conclusions from the crystallization mechanism of one MOF cannot be directly applicable to others. Remarkably, the variation of the HCl/Zr ratio affects not only the crystal size, but also the structure of the formed nodes. At HCl/Zr > 5, the nodes are structurally identical to the  $[Zr_6O_4(OH)_4]$  secondary building units of fully crystalline UiO-66. A HCl/Zr ratio below 5 at Zr/H<sub>2</sub>O ratio of 40 leads to a lower coordination number of Zr atoms, indicative of defective nodes with missing zirconium atoms.

It is important to understand the effect of the composition of the initial synthetic mixture not only on the structural evolution of zirconium-containing species, but also on the state of the organic linker. In the UiO-66, linkers are molecules of deprotonated terephthalic acid, while terephthalic acid is introduced into the synthetic mixture in its protonated form. Moreover, hydrochloric acid is present during the synthesis, therefore shifting the protonation-

deprotonation equilibrium of terephthalic acid to its protonated form. While deprotonation takes place during the UiO-66 synthesis,<sup>[29]</sup> it is unclear whether the protonation/deprotonation equilibrium of the linker affects the kinetics of crystallization and the macroscopic properties of the product.

We applied <sup>1</sup>H and <sup>13</sup>C NMR spectroscopy to investigate the state of the organic linker in the different initial synthetic mixtures. Figure 6 shows <sup>1</sup>H and <sup>13</sup>C NMR liquid-phase NMR spectra corresponding to Series 1 (A and B for <sup>1</sup>H and <sup>13</sup>C NMR spectra, respectively) and Series 2 (C and D for <sup>1</sup>H and <sup>13</sup>C NMR spectra, respectively). <sup>1</sup>H spectra contain signals at 2.87, 3.04 and 8.2 ppm which are assigned to the protons in two methyl groups and the proton attached to the carbonyl group of the DMF molecule, respectively.<sup>[46]</sup> Another signal at 8.3 ppm corresponds to aromatic protons in terephthalic acid, and the signal located between 5 ppm and 7 ppm corresponds to water.<sup>[47]</sup> Notably, the latter becomes sharper and shifts to lower field with an increase in

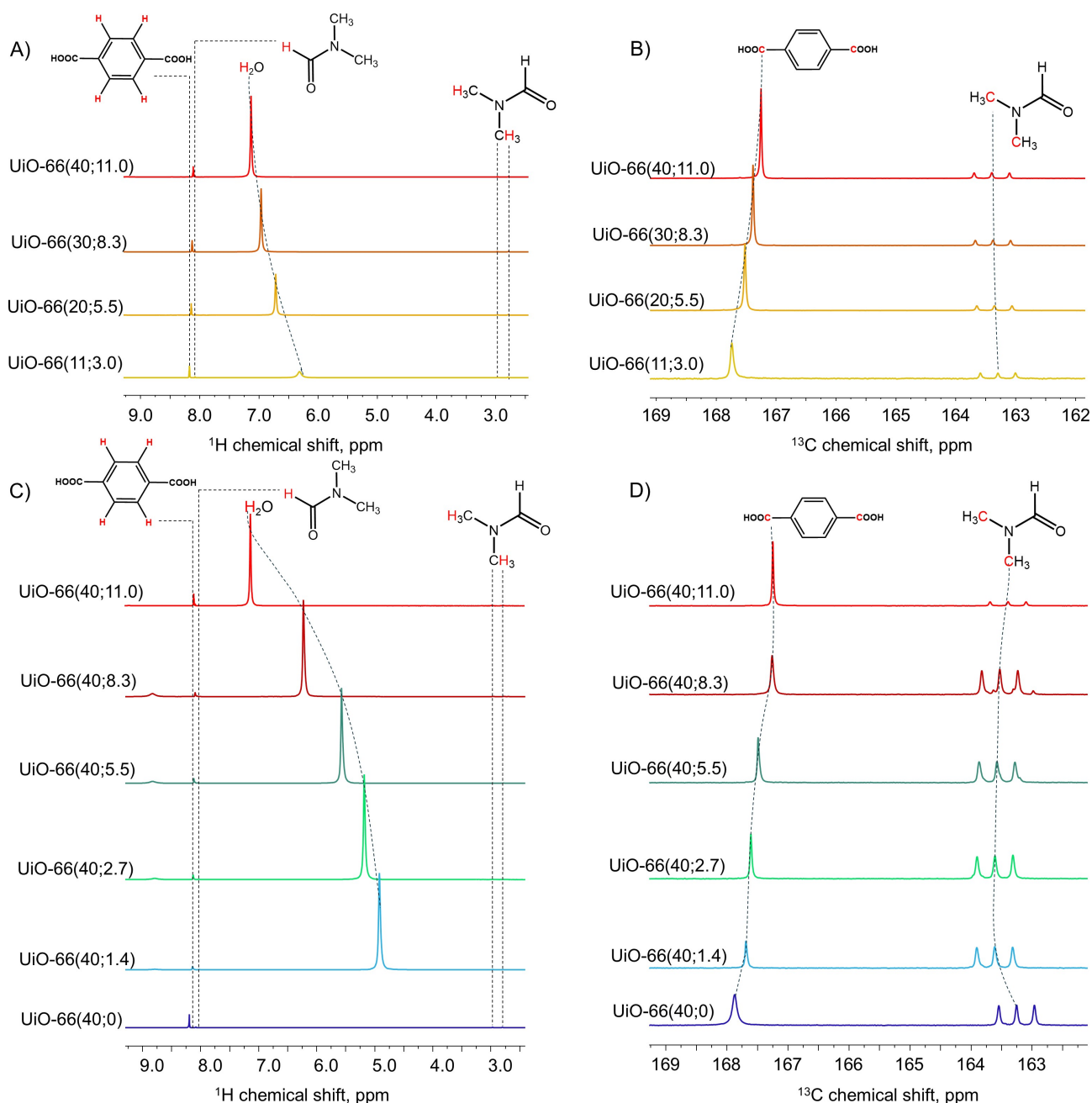


**Figure 6.**  $^1\text{H}$  (A, C) and  $^{13}\text{C}$  (B, D) liquid-phase spectra of initial synthetic mixtures corresponding to Series 1 and 2, respectively. Dotted lines assign signals to corresponding nuclei highlighted in red in the chemical structures.

HCl/Zr and  $\text{H}_2\text{O}$ /Zr ratios in Series 1, and this trend is visible for both series. This is in line with the literature data and confirms an increase in acidity of the synthetic mixture with an increase in HCl concentration.<sup>[48]</sup> In turn,  $^{13}\text{C}$  NMR spectra show the effect of acidity of the synthetic media on the chemical state of the linker. The signal located between 163 and 164 ppm corresponds to the carbonyl group in DMF,<sup>[46]</sup> and the signal between 168 and 167 ppm is due to the carboxylic group in terephthalic acid.<sup>[47]</sup> Notably, the position of the latter signal can be used as a descriptor of the degree of protonation/deprotonation.<sup>[47]</sup> The signal of protonated terephthalic acid is located at 167 ppm, while the

signal of deprotonated terephthalate is shifted to lower field and is centered at around 172 ppm.<sup>[28]</sup> Due to the fast proton exchange, the separate signals of protonated and deprotonated forms are not observed in the actual mixtures; instead, a signal between 167 and 168 ppm is visible with its position indicative of the fraction of deprotonated form. Notably, for Series 1 the increase in HCl/Zr and  $\text{H}_2\text{O}$ /Zr ratios results in a shift of the position of the maximum of the corresponding signal from 167.7 ppm for UiO-66 (11.0, 3.0) to 167.2 ppm for UiO-66 (40.0, 11.0). This suggests a higher degree of protonation of terephthalic acid in synthetic mixtures containing more HCl, as evidenced from  $^1\text{H}$  NMR spectra.

For Series 2, a decrease in HCl/Zr ratio leads to a shift from 167.2 ppm observed for UiO-66 (40.0, 11.0) to 167.8 ppm corresponding to UiO-66 (40.0, 0). Such behavior is also expected: lower HCl concentration leads to a higher degree of dissociation of weak terephthalic acid. Also, this is in line with the results of  $^1\text{H}$  NMR demonstrating a decrease in acidity of the synthetic mixture when smaller amounts of HCl are added. To conclude, our NMR results showed that the increase in HCl concentration leads to the deeper protonation of terephthalic acid.

The presence of water and aqueous hydrochloric acid modulators in the initial synthetic mixture governs both the kinetics of UiO-66 crystallization and the crystal size and the presence of defects of the final product. Applying a comprehensive multi-technique analysis and correlating the macroscopic kinetic trends of crystallization with spectroscopic tracking the fate of zirconium-containing species and linkers during the crystallization, we were able to link the above observed effects to the presence of  $\text{H}_2\text{O}$  and HCl. Figure 7 summarizes the proposed mechanism and shows the effects of both  $\text{H}_2\text{O}$  and HCl.

The synthesis starts with the dissolution of zirconium chloride and the formation of monomeric zirconium species surrounded with preferably chloride ligands and to a lower degree with terephthalate or  $\text{H}_2\text{O}/\text{OH}$  ligands in presumably octahedral coordination characteristic of zirconium complexes in organic solutions<sup>[40]</sup> (Step I in Figure 7). These monomeric zirconium chloride and chloroterephthalate complexes react with water molecules and substitution of chloride ligands with oxygen-containing ones ( $\text{H}_2\text{O}$ ,  $\text{OH}^-$  or bridging  $\text{O}^{2-}$ , possibly also the carboxylic group of tereph-

thalate) takes place (Step II<sub>a</sub> in Figure 7). In the case of high concentrations of water, i.e. high  $\text{H}_2\text{O}/\text{Zr}$  ratios, hydrolysis occurs almost instantaneously (possibly, already during  $\text{ZrCl}_4$  dissolution), and the synthetic mixture contains zirconium-oxo complexes within several minutes after initiation of the synthesis (Step II<sub>b</sub> in Figure 7). These zirconium-oxo complexes exist mostly in a monomeric form, however, hydrolysis initiates the formation of Zr–O–Zr containing structures, leading to a condensation of zirconium-oxo monomers into dimeric and potentially oligomeric species. This stage of hydrolysis of chloroterephthalate zirconium complexes into monomeric and oligomeric oxo-complexes corresponds to the nucleation stage, as evidenced by correlating XRD and XAS data. With condensation further progressing, zirconium monomeric and oligomeric species are transformed into the zirconium-oxo nodes (Step III<sub>a</sub> in Figure 7). Notably, at a HCl/Zr ratio above 5 stoichiometric defect-free  $[\text{Zr}_6(\text{OH})_4\text{O}_4]$  nodes are formed, while at HCl/Zr ratios below 5, the condensation of zirconium species leads to the formation of nodes with missing zirconium atoms (Figure 7, Step III<sub>b</sub>). Notably, these defects do not disappear with extended crystallization time, indicating that the process of nodes formation is irreversible and once formed, nodes with defect do not dissolve and/or heal. The formation of nodes from monomeric and oligomeric species is the rate-limiting step of the crystal growth stage. Further, both defect and defect-free nodes participate in UiO-66 structure formation and are incorporated into the crystal structure on the final stage of crystallization (Step IV in Figure 7). This final stage includes reaction between nodes and terephthalic acid from solution and formation of

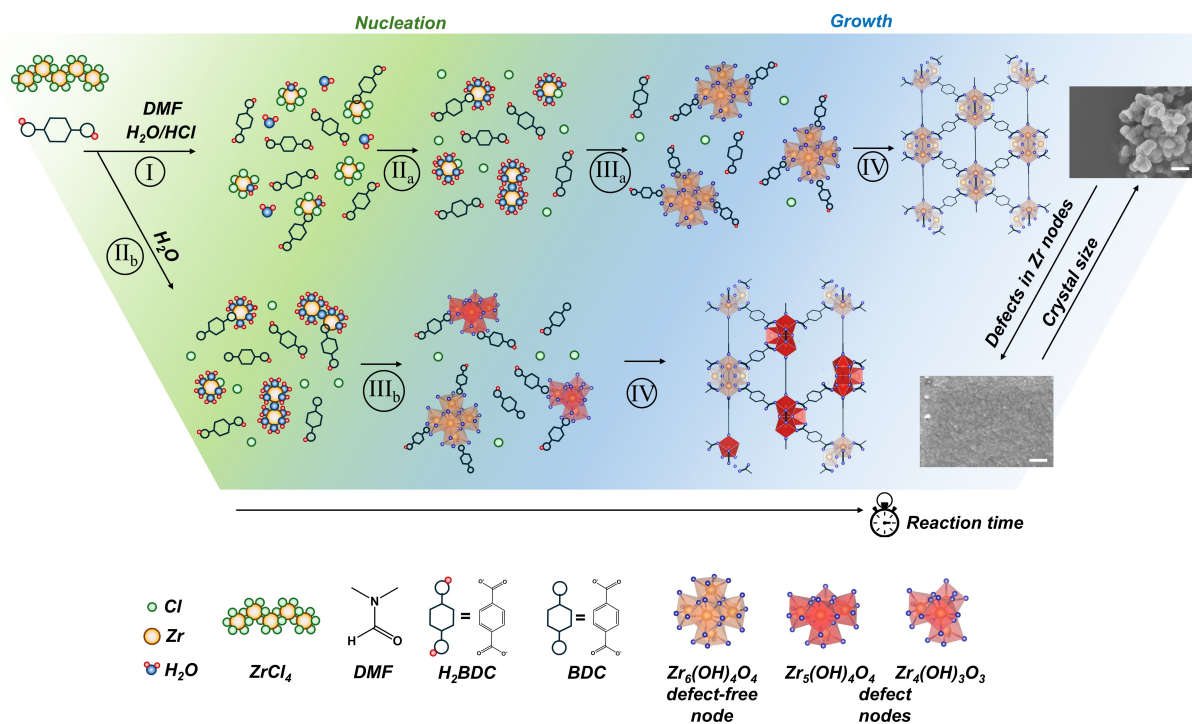


**Figure 7.** Scheme illustrating the chemical transformations taking place during the nucleation and crystal growth phases of UiO-66 crystallization and showing the effect of  $\text{H}_2\text{O}$  and HCl modulators.

the UiO-66. As discussed above, this stage is not rate-limiting in the crystallization, yet some important conclusions regarding this stage can be made. First, as the process is not rate limiting, the degree of terephthalic acid deprotonation cannot determine the growth rate, and this agrees with experimental data. The progressive simultaneous increase in both HCl/Zr and H<sub>2</sub>O/Zr ratios (Series 1) accelerates both nucleation and crystal growth rates, while at the same time, the degree of terephthalic acid deprotonation for Series 1 gradually decreases from UiO-66 (11, 3.3) to UiO-66 (40, 11.0). Thus, the deprotonation of terephthalic acid does not directly affect either nucleation or crystal growth rates. Another important result originates from the fact that the FWHM of XRD peaks does not change after the extent of crystallinity reaches unity. This indicates that the reaction between nodes and linkers leading to a UiO-66 crystal structure is irreversible, making redissolution–crystallization mechanism unapplicable in UiO-66 synthesis, explaining the observed absence of Ostwald ripening.

## Conclusions

Both H<sub>2</sub>O and HCl control the macroscopic and structural properties of UiO-66, such as crystal size, the presence of defects and the kinetics of crystallization from solutions containing ZrCl<sub>4</sub>, DMF and terephthalic acid. This is achieved by influencing both nucleation and crystal growth, more precisely, by affecting the rates of corresponding hydrolysis and condensation reactions, respectively. UiO-66 crystallization implies hydrolysis of zirconium chloride and chloroterephthalate complexes as a rate-limiting step in the nucleation process, and condensation of monomeric and oligomeric zirconium-oxo complexes into nodes, which is the rate-limiting stage of crystal growth. Both processes are irreversible, and both are promoted by H<sub>2</sub>O and inhibited by HCl, however, to a different extent. Nucleation and crystal growth rates are directly proportional to H<sub>2</sub>O/Zr ratio, while inhibition of nucleation by HCl is much more prominent than that of crystal growth. This makes manipulating the H<sub>2</sub>O/HCl ratio a tool to control the relative rates of nucleation and crystal growth, hence enabling control of crystal size of the final product. Notably, fast nucleation in the absence of HCl results in the formation of nodes with missing zirconium atoms. At the final stage of the synthesis both defective and defect-free nodes react with linkers and form the UiO-66. Although this reaction is not rate-limiting and the degree of the deprotonation of terephthalic linker does not influence crystallization kinetics, it is important to note that this transformation is irreversible. This important mechanistic conclusion demonstrates the inapplicability of redissolution–crystallization mechanisms for forming defect free UiO-66. Instead, the defects in the crystal structure are preserved and cannot be (self) healed through prolongation of the crystallization time.

From a methodological perspective, the combination of advanced in situ techniques and precise experiment planning with comprehensive variation of the synthetic parameters was needed to determine the detailed molecular-level

mechanism of solvothermal synthesis of solid materials and avoid ambiguous and erroneous conclusion.

## Acknowledgements

The authors thank the SLS for providing beamtime at the SuperXAS beamline. A part of the reported data was collected within the “Cook and Look: watching functional materials in situ” ETH course at SLS, we thank the class of 2022 for their help. The authors acknowledge the assistance of Mr. Andreas Brenig during the XAS beamtime.

## Conflict of Interest

The authors declare no conflict of interest.

## Data Availability Statement

The data that support the findings of this study are available from the corresponding author upon reasonable request.

**Keywords:** MOF synthesis · crystallization · nucleation · defects · in situ spectroscopy

- [1] H. C. Zhou, J. R. Long, O. M. Yaghi, *Chem. Rev.* **2012**, *112*, 673–674.
- [2] H. Furukawa, K. E. Cordova, M. O’Keeffe, O. M. Yaghi, *Science* **2013**, *341*, DOI: 10.1126/science.1230444.
- [3] H. C. J. Zhou, S. Kitagawa, *Chem. Soc. Rev.* **2014**, *43*, 5415–5418.
- [4] W. Lu, Z. Wei, Z. Y. Gu, T. F. Liu, J. Park, J. Park, J. Tian, M. Zhang, Q. Zhang, T. Gentle, M. Bosch, H. C. Zhou, *Chem. Soc. Rev.* **2014**, *43*, 5561–5593.
- [5] A. Kirchon, L. Feng, H. F. Drake, E. A. Joseph, H. C. Zhou, *Chem. Soc. Rev.* **2018**, *47*, 8611–8638.
- [6] H. Li, K. Wang, Y. Sun, C. T. Lollar, J. Li, H. C. Zhou, *Mater. Today* **2018**, *21*, 108–121.
- [7] M. P. Suh, H. J. Park, T. K. Prasad, D. W. Lim, *Chem. Rev.* **2012**, *112*, 782–835.
- [8] J. R. Li, J. Sculley, H. C. Zhou, *Chem. Rev.* **2012**, *112*, 869–932.
- [9] L. Zhu, X. Q. Liu, H. L. Jiang, L. B. Sun, *Chem. Rev.* **2017**, *117*, 8129–8176.
- [10] W. Liu, X. B. Yin, *TrAC Trends Anal. Chem.* **2016**, *75*, 86–96.
- [11] P. Horcajada, R. Gref, T. Baati, P. K. Allan, G. Maurin, P. Couvreur, G. Férey, R. E. Morris, C. Serre, *Chem. Rev.* **2012**, *112*, 1232–1268.
- [12] L. Valenzano, B. Civalieri, S. Chavan, S. Bordiga, M. H. Nilson, S. Jakobsen, K. P. Lillerud, C. Lamberti, *Chem. Mater.* **2011**, *23*, 1700–1718.
- [13] A. Dhakshinamoorthy, A. Santiago-Portillo, A. M. Asiri, H. Garcia, *ChemCatChem* **2019**, *11*, 899–923.
- [14] M. Kadhom, M. Al-Furaiji, S. Salih, M. A. Al-Obaidi, G. H. Abdullah, N. Albayati, *J. Water Proc. Eng.* **2023**, *51*, 103402.
- [15] J. Winarta, B. Shan, S. M. McIntyre, L. Ye, C. Wang, J. Liu, B. Mu, *Cryst. Growth Des.* **2020**, *20*, 1347–1362.
- [16] Q. Yang, H. Jobic, F. Salles, D. Kolokolov, V. Guillermin, C. Serre, G. Maurin, *Chem. A Eur. J.* **2011**, *17*, 8882–8889.
- [17] J. Qiu, Y. Feng, X. Zhang, M. Jia, J. Yao, *J. Colloid Interface Sci.* **2017**, *499*, 151–158.

- [18] F. Ragon, P. Horcajada, H. Chevreau, Y. K. Hwang, U. H. Lee, S. R. Miller, T. Devic, J. S. Chang, C. Serre, *Inorg. Chem.* **2014**, *53*, 2491–2500.
- [19] L. Chu, J. Guo, L. Wang, H. Liu, J. Yan, L. Wu, M. Yang, G. Wang, *Appl. Organomet. Chem.* **2022**, *36*, e6559.
- [20] B. P. Carpenter, A. R. Talosig, B. Rose, G. Di Palma, J. P. Patterson, *Chem. Soc. Rev.* **2023**, *52*, 6918–6937.
- [21] M. Taddei, N. Casati, D. A. Steitz, K. C. Dübngen, J. A. van Bokhoven, M. Ranocchiari, *CrystEngComm* **2017**, *19*, 3206–3214.
- [22] L. S. Germann, A. D. Katsenis, I. Huskić, P. A. Julien, K. Užarević, M. Etter, O. K. Farha, T. Frišćić, R. E. Dinnebier, *Cryst. Growth Des.* **2020**, *20*, 49–54.
- [23] M. J. Van Vleet, T. Weng, X. Li, J. R. Schmidt, *Chem. Rev.* **2018**, *118*, 3681–3721.
- [24] M. Avrami, *J. Chem. Phys.* **1941**, *9*, 177–184.
- [25] J. D. Hancock, J. H. Sharp, *J. Am. Ceram. Soc.* **1972**, *55*, 74–77.
- [26] A. F. Gualtieri, *Phys. Chem. Miner.* **2001**, *28*, 719–728.
- [27] H. Xu, S. Sommer, N. L. N. Broge, J. Gao, B. B. Iversen, *Chem. A Eur. J.* **2019**, *25*, 2051–2058.
- [28] D. Salionov, O. O. Semivrazhskaya, N. P. M. Casati, M. Ranocchiari, S. Bjelić, R. Verel, J. A. van Bokhoven, V. L. Sushkevich, *Nat. Commun.* **2022**, *13*, 1–9.
- [29] O. O. Semivrazhskaya, D. Salionov, A. H. Clark, N. P. M. Casati, M. Nachtegaal, M. Ranocchiari, S. Bjelić, R. Verel, J. A. van Bokhoven, V. L. Sushkevich, *Small* **2023**, *19*, 2305771.
- [30] G. Zahn, P. Zerner, J. Lippke, F. L. Kempf, S. Lilienthal, C. A. Schröder, A. M. Schneider, P. Behrens, *CrystEngComm* **2014**, *16*, 9198–9207.
- [31] C. S. Cox, E. Slavich, L. K. Macreadie, L. K. McKemmish, M. Lessio, *Chem. Mater.* **2023**, *35*, 3057–3072.
- [32] X. Feng, H. S. Jena, C. Krishnaraj, K. Leus, G. Wang, H. Chen, C. Jia, P. Van Der Voort, *ACS Appl. Mater. Interfaces* **2021**, *13*, 60715–60735.
- [33] S. Ali, Z. Zuhra, Y. Abbas, Y. Shu, M. Ahmad, Z. Wang, *Langmuir* **2021**, *37*, 13602–13609.
- [34] X. Chen, Y. Li, Q. Fu, H. Qin, J. Lv, K. Yang, Q. Zhang, H. Zhang, M. Wang, *RSC Adv.* **2022**, *12*, 6083–6092.
- [35] S. E. Massimi, K. E. Metzger, C. M. McGuirk, B. G. Trewyn, *Inorg. Chem.* **2022**, *61*, 4219–4234.
- [36] S. R. Wasserman, *J. Phys. IV JP* **1997**, *7*, C2–203.
- [37] S. Beauchemin, D. Hesterberg, M. Beauchemin, *Soil Sci. Soc. Am. J.* **2002**, *66*, 83–91.
- [38] J. H. Cavka, S. Jakobsen, U. Olsbye, N. Guillou, C. Lamberti, S. Bordiga, K. P. Lillerud, *J. Am. Chem. Soc.* **2008**, *130*, 13850–13851.
- [39] K. A. Lomachenko, J. Jakobsen, A. L. Bugaev, C. Atzori, F. Bonino, S. Bordiga, N. Stock, C. Lamberti, *J. Am. Chem. Soc.* **2018**, *140*, 17379–17383.
- [40] M. Kløve, R. S. Christensen, I. G. Nielsen, S. Sommer, M. R. V. Jørgensen, A. C. Dippel, B. B. Iversen, *Chem. Sci.* **2022**, *4*, 12883–12891.
- [41] R. E. Connick, W. H. Reas, *J. Am. Chem. Soc.* **1951**, *73*, 1171–1176.
- [42] C. Ekberg, G. Källvenius, Y. Albinsson, P. L. Brown, *J. Solution Chem.* **2004**, *33*, 47–79.
- [43] M. Taddei, J. A. okhoven, M. Ranocchiari, *Inorg. Chem.* **2020**, *59*, 7860–7868.
- [44] M. Taddei, K. C. Dübngen, J. A. van Bokhoven, M. Ranocchiari, *Chem. Commun.* **2016**, *52*, 6411–6414.
- [45] M. Filez, C. Caratelli, M. Rivera-Torrente, F. Muniz-Miranda, M. Hoek, M. Altelaar, A. J. R. Heck, V. Van Speybroeck, B. M. Weckhuysen, *Cell Reports Phys. Sci.* **2021**, *2*, 100680.
- [46] E. G. V. K. A. Nudelman, *J. Org. Chem.* **1997**, *3263*, 7512–7515.
- [47] Y. Kosugi, T. Takeuchi, *J. Magn. Reson.* **1978**, *32*, 83–88.
- [48] Y. Yasaka, C. Wakai, N. Matubayasi, M. Nakahara, *Anal. Chem.* **2009**, *81*, 400–407.

Manuscript received: August 20, 2024

Accepted manuscript online: November 28, 2024

Version of record online: December 9, 2024